Hilbert fractal acoustic metamaterial with negative mass density and bulk modulus on subwavelength scale

Xianfeng Man [a,b], Zhen Luo [b], Jian Liu [a], Baizhan Xia [a,*]
[a] State Key Laboratory of Advanced Design and Manufacturing for Vehicle Body, Hunan University, Changsha, Hunan 410082, China
[b] School of Mechanical and Mechatronic Engineering, University of Technology Sydney, Sydney, NSW 2007, Australia

Abstract

Acoustic metamaterials (AMs) are an artificial structure/material which can offer great flexibility for manipulating the wave propagation by its unconventional equivalent properties, which can produce a broad applications such as sound cloaking and tunneling et al.. In nature, bio-inspired fractal organization with multiple length scales has been found in various biological materials, which display enhanced dynamic properties. In this work, by introducing *Hilbert curve* channels, we design a class of topological architectures of Hilbert fractal acoustic metamaterials (HFAMs) with negative mass density and bulk modulus on subwavelength scale. Here, we highlight the influences of the self-similar fractal configurations on multipole modes of HFAM. To further demonstrate multipole resonances, the pressure magnifications are examined in the center region of HFAM with losses. Furthermore, based on effective medium theory, we systematically calculate and investigate negative bulk modulus and mass density, and density-near-zero of HFAM, which demonstrate the sound blocking and the zero-phase-difference effects of HFAMs on subwavelength scale. Numerical results show that HFAM makes it a good candidate for a number of applications, from sound blocking, quarter bending, sound cloaking to sound tunneling, and may further provide a possibility for the engineering applications of the exotic properties on subwavelength scale.

* Corresponding author.
E-mail: xiabz2013@hnu.edu.cn (B.Z. Xia)

Keywords: Hilbert fractal acoustic metamaterials, Degative mass density, Degative bulk modulus, Sound blocking, Zero-phase-difference

Nomenclature		a_0	lattice constant
		N	fractal order
a	length of the unit cells	H', H'', H'''	solid wall thicknesses
K	Hilbert channel width	ρ_1/ρ_0	materials/air density
D_f	fractional dimension	c_1/c_0	materials/air sound speed
l	feature segment	L	Euclidean total length of fractal waveguide
n_{eff1}, n_{eff2}, n_{eff3}	effective refractive index of the first to third order HFAM	L_{eff1}, L_{eff2}, L_{eff3}	sound propagation length of the first to third order HFAM
k	wave number	λ	sound wave wavelength
f	frequency	ω	angular frequency
fa_0/c_0	the normalized frequency	$\boldsymbol{r}$	position vector
t	time	p_0	a unit sound pressure
k_{eff}	effective wave number	p_{in}	a harmonic oscillation
Z_{eff}	effective impedance	P_1/P_2	complex pressures on left/right faces
ρ_{eff}	effective dynamic mass density normalized to background air	V_1/V_2	complex normal acoustic particle velocities on left/right faces
B_{eff}	effective dynamic bulk modulus normalized to background air	P_{x1}, P_{x2}, P_{x3}, P_{x4}	four positions complex sound pressures
d_e	a unit cell layer	$\boldsymbol{T}_e$	transfer matrix
A/B	amplitudes coefficients of the acoustic waves	L_1, L_2	distances of P_{x2} and left slab, P_{x3} and right slab
T	transmission coefficient	R	reflection coefficient
d	multiple units slab thickness	S_1, S_2	distances of P_{x1} and P_{x2}, P_{x3} and P_{x4}

1. Introduction

AMs are artificial materials/structures designed to exhibit unconventional effective properties that are usually not associated with ordinary composites. AMs analogue to electromagnetic metamaterials have already been investigated in recent works, such as negative effective parameters [1,2], negative refractive index or near-zero-index [3,4], energy absorption [5,6], absorber [7-9], acoustic cloaking [10,11], acoustic superlens [12,13] and topologically protected one-way propagation [14]. So far, most of AMs can

primarily be divided into locally resonant acoustic metamaterials (LRAMs) with basic resonators [2,15], membrane-type AMs [1] and other types of AMs based on effective medium theory [16,17].

For instance, in 2000, Liu et al. [15] first fabricated and investigated an AMs that exhibits negative elastic constants with a lattice constant two orders of magnitude smaller than the operating wavelength based on LR structures. In 2004, Li et al. [18] theoretically demonstrated a simultaneously negative effective bulk modulus and mass density by dispersing periodic array of soft rubber in water. Fang et al. [2] investigated the dynamic behaviors and the effective parameters of the Helmholtz resonant AMs. Since then, AMs with the single and double negative properties by LRAMs have gained more attention [19-22]. By introducing the periodic arrangement of Helmholtz resonators, Lee et al. [19] first experimentally demonstrated acoustic double negativity of an AM with an array of side holes on a tube. Yang et al. [23] proposed a new LRAM, so-called the membrane-type AMs with the negative dynamic mass. For LRAMs, their absorption losses are usually considerable and their responses associated with a low symmetry are generally anisotropic. Furthermore, it is still a considerably technological challenge to encapsulate the high-density particles in a soft matrix material with a highly stable shape and a well controllable arrangement. These inherent drawbacks seriously restrict the practical applications of LRAMs.

To overcome these defects, recently, the researchers introduce the space-coiling technique into AMs, and design the labyrinthine/space-coiling AMs with a geometry-based mechanism [24-29]. It provides a novel mechanism that the sound wave transmits along the space-coiling instead of a straight line. This enables the propagation length of wave to be multiplied, increasing the total propagation time and decreasing the effective phase velocity. These labyrinthine AMs have an extremely low absorption loss and a high refractive index. For example, Liang et al. [24,26] firstly designed the space-coiling AMs and confirmed the negative refractive index and the dispersive characteristics. Li et al. [25] designed an AM with curled channels to achieve an acoustic gradient len with arbitrarily large refractive index and greatly high

transmission efficiency. Xie et al. [27,28] shown the appearance of the broadband negative refractive index and the broadband impendance matching in a labyrinthine AM. Frenzel et al. [29,31] designed the zig-zag channels to achieve the broadband sound attenuation and the double negativity in a three-dimensional (3D) labyrinthine AM. Cheng et al. [32] proved the high reflection of the low-frequency sound in an artificial Mie-resonance-based AMs consisting of the zig-zag channels. Subsequently, a class of AMs with labyrinthine structures or Mie-resonances was further developed in many applications, such as the sound absorption and blocking [33], acoustic focusing lens [25], high transmission [34], directional sensing [35,36], acoustic cloaking and tunneling [37]. To date, AMs are restricted to the simple zigzag channels or inspirations of natural biological structure/materials, which have certain contingency. The structure complexity of AMs is endless. Hence, how to design geometric structures or bio-inspired configurations with appropriate and precise mathematical formulas, so as to achieve the unusual characteristics of the labyrinthine AMs, is of great importance to broaden the practical applications.

The self-similar fractal structures and their applications are ubiquitous in the biological and mechanical territories [38]. Inspired by the fractal and "pseudo-fractal" architectures, the hierarchical phononic crystals with the fractal organizations have been explored [39-41]. Recent researches involving acoustic/elastic waves have shown the hierarchical and fractal-like AMs can provide superior wave attenuation in multiband or deep-subwavelength scale due to their unique structures [42-50]. Song et al. [42] fabricated a broadband fractal AMs that can shield the low-frequency sounds at specific frequencies. Man et al. [46] proposed a kind of HFAM to investigate the effects of the fractal order on the band structures and the wavefront shaping. The results shown that with the increase of fractal order, the total width of bandgaps increases, and the deep-subwavelength bandgap appears. Furthermore, with properly arranged HFAMs, it can flexibly reshape the plane waves from the high to low frequency range. For the higher order HFAMs, it shows good robustness against the irregular arrangements in sound transmission. Krushynska et al. [47] designed a labyrinthine AM with the

Wunderlich sub-wavelength paths, based on self-similar organization, as efficient reflectors to control low-frequency airborne sound. Zhao et al. [49] and Man et al. [50] designed the stretched and 3D HFAM respectively to control the ultra low frequency and multiband acoustic insulation. Other related studies have also been reported on controlling propagation of sound waves by the fractal AMs, such as broadband wave filtering [51,52], broadband focusing acoustic lens [43].

Despite these considerable efforts, the challenges still exist. For example, almost all of them focus on the sound blocking, as mentioned above articles. In Ref [46], the proposed HFAM units were exploited to explore sound blocking by the multi-bandgaps characteristics, and the wavefront shaping effect was achieved only by the simulation. However, the numerical solutions of the density-near-zero and other applications of HFAMs, like sound cloaking and tunneling were not explored yet. In addition, to our best knowledge, the labyrinthine fractal AMs with negative bulk modulus and mass density have seldom been investigated. Moreover, the existing design methods for the labyrinthine fractal AMs are lack of rigorous mathematical models, limiting the fractal orders of the configuration. The multi-scale self-similar fractal models will greatly enrich the design method for AMs.

As an effort to fill in the above-mentioned research gaps, this work will introduce the effect of the self-similar fractal on HFAM with the negative mass density and bulk modulus on subwavelength scale. The significances of the present study can be summarized as the following: (1) the proposed subwavelength HFAMs are capable of producing the rich multipole resonances. The significant effects of the fractal-inspired hierarchies on the distributions of the pressure and phase fields of the multipole modes are systematically investigated. To further demonstrate resonances characteristics, the pressure magnifications in the center region of HFAM are explored in the presence of the air losses; (2) Based on effective medium theory, the negative effective parameters and density-near-zero of HFAM are numerically calculated on subwavelength scale. Meanwhile, the relationships of the negative mass density and bulk modulus and the width of *Hilbert curve* channel are discussed; (3) By the properties of the negative

effective parameters, the designed HFAMs with the sparse arrangement are used for multi-band sound blocking on subwavelength scale. Finally, the effectiveness and applications of HFAMs with the density-near-zero feature are demonstrated in the zero-phase-difference phenomena, like the quarter bending, sound cloaking and tunneling.

2. Design, mechanism and eigenstate modes of HFAM

2.1. Design of unit cells of HFAM

The 2D unit cells of the first order, the second order and the third order HFAM, are respectively illustrated in Fig. 1. In the design of HFAM, a square with a side length of $a/2$ is divided into 2^1-by-2^1 section. The centers of 2^1-by-2^1 section are connected from the lower-left and lower-right in a clockwise direction, opening a width of *K Hilbert curve* channel, as indicated in Fig. 1(a). As the fractal order increases, the squares of $a/2$ are divided into 2^2-by-2^2 and 2^3-by-2^3 section, respectively, as given in Fig. 1(b) and (c). Fig. 1(d)-(f) represent the units of the first to third order HFAM [46]. The proposed configurations include a square frame and are divided into four sectors with independent curved channels connected at the center. For simplicity, each order curve has a length $a/2$, and the feature segment (i.e., the shortest segment) length of the N-order Hilbert structure is $l = a/2^{N+1} (N = 1,2,3)$. Therefore, the Euclidean total length of fractal waveguide is $L = 2^{N-1}a - l\ (N = 1,2,3)$. In addition, the sound wave propagation length within a unit cell with *Hilbert curve* channel is $L_{\text{eff}} = (2^{N-1} - \frac{1}{2^{N+1}} + \frac{\sqrt{2}+1}{2^{N+2}})a\ (N = 1,2,3)$.

This *Hilbert curve* eventually fills the entire square area, if fractal order $N \to \infty$ [53]. Here, considering sound channel of HFAM instead of Hilbert curve, so it can not be fractal infinitely in a constant square. With the increase of fractal order, the thicknesses (H', H'', H''' and W', W'', W''') of the structure walls become thinner shown in Fig. 1(d)-(f), hence we can find that the higher of the fractal order, the lighter of HFAM

weight. Thus, the higher order HFAM is easier to achieve the lightweight characteristic.

2.2. Mechanism and eigenstate modes of HFAM

Unlike the mechanism of the Helmholtz resonator-based AMs [2] and the membrane-based AMs [1,23], the labyrinthine AMs are excited by an ultra-slow acoustic medium with a high refractive index, when compared with the background medium [24-33]. In HFAM, the sound waves propagate along *Hilbert curve* channels instead of straight lines, so the total propagation length of sound wave is multiplied. Thus, the effective speed of air particle within HFAM is ultraslow, and it can be efficiently equivalent to an artificial medium with a higher refractive index. The effective refractive index n_{eff} is evaluated as the ratio between the approximate total length of the sound wave path inside *Hilbert curve* channel and the length of the inlet and center connected by a straight line in Fig. 1. A rough estimation of n_{eff} of HFAM unit can be formulated as

$$n_{eff} \approx \frac{L_{eff}}{a/2} = \frac{(2^N - \frac{1}{2^N} + \frac{\sqrt{2}+1}{2^{N+1}})a}{a} \ (N=1,2,3)\,. \tag{1}$$

Here, sound wave propagates along the *Hilbert curve* channel, n_{eff} of HFAM are much larger than 1 (n_{eff1}=2.2, n_{eff2}=4.2, n_{eff3}=7.8). In this study, we consider that HFAM units are uniformly arranged in a square lattice, whose lattice constants are a_0=110 mm.

HFAM can stimulate abundantly resonance modes, such as the monopole and multipole resonances. We study the eigenstates of HFAM by COMSOL eigenfrequency module with the periodic boundary conditions. The monopole resonance can lead to a negative bulk modulus, while the dipole resonance can lead to a negative mass density [32]. The eigenstates of HFAM are shown in Fig. 2, in which the monopolar and dipolar resonance frequencies of the first, second, third order HFAM are 586 Hz and 1343 Hz, 389 Hz and 806 Hz, 228 Hz and 461 Hz, respectively. For the monopole modes of HFAM, in Fig. 2((a) and (c), (e) and (g), (i) and (k)), the sound energies mainly concentrate at the interconnection center of HFAM and radiate sound equal approximately in four *Hilbert curve* channels directions, and the phases in these

directions are the same. These results indicate that the sound wave simply moves inward and outward in a collective in-phase pattern which is independent of the directions of propagation. Fig. 2((b) and (d), (f) and (h), (j) and (l)) depicts the dipole modes of HFAM, the sound energies concentrate in the opposite sides (the upper-left and lower-right channels) of HFAM, and their phases have a difference of π. The sound waves along the opposite directions are out-phase pattern with one inward and the another outward.

Hence, the designed HFAM can control the behaviors of monopole and dipole modes. In addition, with the increasing the fractal order, the monopole and dipole frequencies of the third order HFAM are shifted to lower frequency range. Its normalized frequencies of the monopole and dipole resonances are 0.073 and 0.148, respectively. Note that the third order HFAM is a deep-subwavelength structure and provides an alternative route to control the propagation of the sound wave with a wavelength as long as nearly 1.5 m.

Numerical simulation with COMSOL Multiphysics, a FEM analysis and solver software, is further performed to prove the monopole and dipole resonances with the frequency-domain model schematically depicted in Fig. 3(a). The calculations are performed here with respect to the pressure magnification in the region of the interconnection center of HFAM. The pressure amplifications are calculated based on the average values of the central regions (yellow part) as displayed in Fig. 3(a). We consider the propagation of plane wave governed by the Helmholtz equation:

$$\nabla\left(-\frac{1}{\rho_0}\nabla p_0\right)-\frac{\omega^2}{\rho_0 c^2}p_0=0. \tag{2}$$

A harmonic oscillation $p_{in}=p_0e^{i\omega t}$ with angular frequency ω and a unit amplitude p_0=1 Pa is impacted on the left boundary, where the source excitation is applied to simulate sound plane waves. At the top and bottom boundaries, the Floquet-Bloch periodic conditions ($p_0(\boldsymbol{r}+a_0)=p_0(\boldsymbol{r})e^{-\boldsymbol{k}a_0}$) are applied to simulate an infinite medium in y-direction in Fig. 3(a). In addition, considering that the material's impedance is much larger than that of air, the solid walls can be regarded as the sound-hard boundary condition [29,34]. The Perfectly Matched Layer (PML) is

performed on the outlet of the waveguide to eliminate the reflected waves. In addition, when acoustic waves propagate through *Hilbert curve* channels with small dimensions, the air losses should be considered [32,54].

As predicted in Fig. 2(a), (e), (i), the localized pressures in the interconnection center of HFAM should increase significantly at the monopolar frequency. This behaviour is clearly proved by the pressure magnifications in the region of the interconnection center of HFAM, as shown in Fig. 3(b)-(d). Fig. 3(b) shows that the maximum magnification of the first order HFAM occurs at 591 Hz with a pressure enhancement of 9.2 times in simulations with lossless. The sound pressure field concentrates in the center around monopole resonance (Fig. 2(a)). Note that there is a small peak and dip around 1300 Hz, in which sound pressure field radiates in the opposite directions (Fig. 2(b)). The two peaks of pressure magnification confirm the monopole and dipole modes, depicted in Fig. 2(a) and (b). Fig. 3(c) shows that the maximum magnification of the second order HFAM occurs at 395 Hz with a pressure enhancement of 10.1 times. It is noteworthy that there was a small peak and dip around 801 Hz when the pressure magnification equal to one. The two peaks of pressure magnification validate the monopole and dipole mode, shown in Fig. 2(e) and (f). Fig. 3(d) shows the maximum magnification of the third order HFAM occurs at 229Hz with a pressure enhancement of 9.7 times. Note that there is a small peak and dip around 456 Hz when the pressure magnification equal to one. The two peaks of pressure magnification confirm the monopole and dipole mode, displayed in Fig. 2(i) and (j). These results are shown in Fig. 3(b)-(d), at resonance frequencies 591 Hz and 1300 Hz, 395 Hz and 801 Hz, 229 Hz and 456 Hz, which agree with the monopolar and dipolar resonances modes of HFAM displayed in the Fig. 2, respectively.

To further illustrate the effect of losses, the pressure magnifications in the interconnection center of HFAM with respect to different losses are shown in Fig. 3(b)-(d). It is clearly observed that peaks of the pressure magnifications of HFAM around the monopole resonance frequencies decrease sharply and their corresponding frequencies are not shifted as a consequence of losses. The peaks and dips of pressure magnification have a small decrease near the dipole resonance frequencies. Moreover, the pressure magnifications in the monopole and dipole modes associated with sound blocking behavior are partly suppressed due to losses effect. The insets of monopole and dipole mode with loss=0.032 as shown in Fig. 3(b)-(d), they indicate that amplitudes of pressure field distributions encounter the reduction in any position.

As mentioned above, these results imply that the monopole and dipole resonances obtained based on eigenstate and frequency-domain calculations are almost consistent, except for the dipole resonance of the first order HFAM. Specifically, as compared with the first two orders, in the vicinity of monopole resonance, the third order HFAM not only can obtain convergence of wave energy, but also can regulate sound wavelength with 13.6 times larger than unit dimension in deep-subwavelength scales.

2.3. Effects of Hilbert curve channel on resonant modes

Here, we consider the influence of *Hilbert curve* channels K on the monopole and dipole resonance, and pressure magnification of monopole modes, shown in Fig. 4. Firstly, for the first two orders, with the increase of K, it can be seen that the monopole resonances gradually increase and tend to stabilize, while the dipole resonances first decrease and then increases in Fig 4(a) and (b). Secondly, the monopole and dipole resonances of the third order HFAM are increasing gradually in Fig 4(c). Fig. 4(d)-(e) show the pressure magnifications of monopole resonance in the interconnection center of HFAM. From the figure, it is clear that pressure magnifications of HFAM drop rapidly, and then slowly, as the K increases. The second and third order HFAM with a longer path have much higher-pressure magnifications, which even approach to the enhancement of 50 times, when the K≈1mm. It indicates that the amount of energy radiated outward less and is largely concentrated in the central area. Thus, we enable to change the geometrical parameter of HFAM, such as decreasing the width of *Hilbert curve* channel, so that the more sound energy of the interconnection center can be concentrated in a low-frequency range. It may have a good prospect in the application of energy collection in the presence of losses.

3. Effective parameters of unit cell of HFAM: ρ_{eff} and B_{eff}

3.1. Transfer matrix method

To provide a deep insight into the physical properties of HFAM, its effective parameter is systematically calculated by the transfer matrix method, which has been widely used in the past to analyze and measure acoustical properties of porous materials [55]. Under the long-wavelength assumption, the structure can be equivalent to a homogeneous and isotropic medium can be considered to calculate the effective parameters of wave propagation characteristics [56].

Here, the transfer matrix is used to relate the sound pressures and normal acoustic particle velocities on the two faces of a unit layer extending from x=0 to x=d_e as in Fig. 5(a), i.e.,

$$\begin{bmatrix} P_1 \\ V_1 \end{bmatrix}_{x=0} = \boldsymbol{T}_e \begin{bmatrix} P_2 \\ V_2 \end{bmatrix}_{x=d_e}, \tag{3}$$

Where P_i and V_i are the complex pressures and complex normal acoustic particle velocities on the two faces of the effective medium, they are expresses as:

$$\begin{cases} P_i = (Ae^{-ik_{eff}x} + Be^{ik_{eff}x})_x \\ V_i = \dfrac{1}{\rho_{eff}c_0}(Ae^{-ik_{eff}x} - Be^{ik_{eff}x})_x \end{cases}, \tag{4}$$

The coefficients A and B are the amplitudes of acoustic waves. By combining Eqs. (3) and (4), the transfer matrix can be expressed directly in terms of the pressures and velocities on the two surfaces of the unit layer, i.e.,

$$\boldsymbol{T}_e = \begin{bmatrix} T_{11} & T_{12} \\ T_{21} & T_{22} \end{bmatrix} = \begin{bmatrix} \cos k_{eff}d_e & j\rho_{eff}c_0 \sin k_{eff}d_e \\ j\sin(k_{eff}d_e)/\rho_{eff}c_0 & \cos k_{eff}d_e \end{bmatrix}, \tag{5}$$

Where $k_{eff} = (1/d_e)\cos^{-1}T_{11}$ is a complex wave number, and the complex characteristic impedance can be calculated from the showed matrix equation, $Z_{eff} = \rho_{eff}\omega / k_{eff}$. The effective mass ρ_{eff} and bulk modulus B_{eff} are given by Eq. (5) and dispersion relation [56].

$$\rho_{eff} = \frac{jk_{eff}\sin k_{eff}d_e}{\omega T_{21}} \Big/ \rho_0, \; B_{eff} = \frac{\omega^2}{k_{eff}/\rho_{eff}} \Big/ \rho_0 c_0^2. \tag{6}$$

Where ρ_{eff} and B_{eff} are the effective parameters normalized to background air, respectively.

3.2. Double negative HFAM: ρ_{eff} and B_{eff}

The calculated responses of ρ_{eff} and B_{eff} by transfer matrix method are shown in Fig. 5(b)-(d), respectively. Fig. 5(b) illustrates ρ_{eff} and B_{eff} of unit cell of the first order HFAM. In the frequency ranges [609 Hz, 792 Hz] and [1192 Hz, 1400 Hz], the values of B_{eff} and ρ_{eff} change from positive value to negative one, respectively, as the

monopolar and dipolar resonance occur in Fig. 2(a)-(b). In the vicinity of the monopole resonant frequency, B_{eff} is negative where the external pressure and the volume change are out of phase. In the vicinity of the dipole resonant frequency, ρ_{eff} is negative where the acceleration response is opposite to the external excitation [32]. Fig. 5(c) illustrates ρ_{eff} and B_{eff} of unit cell of the second order HFAM. In the frequency ranges [408 Hz, 549 Hz] and [749 Hz, 866 Hz], the values of B_{eff} and ρ_{eff} switch to be negative one, as the monopole and dipole resonance occur in Fig. 2(e)-(f).

Fig. 5(d) illustrates ρ_{eff} and B_{eff} of unit cell of the third order HFAM. In the frequency ranges [230 Hz, 311 Hz] and [386 Hz, 474 Hz], the values of B_{eff} and ρ_{eff} switch to negative one, as the monopolar and dipolar resonance occur in Fig. 2(i)-(j). At frequencies near resonance, a considerable amount of energy is stored in the structure. Note that ρ_{eff} have two peaks, one is caused by the couple of antiresonance behaviour of ρ_{eff} and resonance behaviour of B_{eff}, which has been proven previously [32]. By varying the size and *Hilbert curve* channel, we can tune the B_{eff} and ρ_{eff} to negative values at desired frequency ranges. The air loss=0.0093 is assumed in the simulations of ρ_{eff} and B_{eff}. It is clearly seen that the loss influences the peaks and dips of B_{eff} in the vicinity of the monopole frequency. The peaks of negative B_{eff} are sharply reduced. Corresponding to the pressure magnification in the region of the interconnection center in the insert of Fig. 3, the accumulations of energy are decreased in the structure. ρ_{eff} crosses zero and the corresponding frequencies are slightly shifted. The peaks of negative ρ_{eff} are also sharply reduced.

In addition, the resonant modes are dependent on the width of *Hilbert curve* channel *K*. Fig. 6 depicts the negative ρ_{eff} and B_{eff} of HFAM with respect to *Hilbert curve* channel *K*. It should be noticed that as the width *K* increases, the range of negative ρ_{eff} and B_{eff} also widens respectively. Interestingly, as observed in Fig. 6(a)-(b), when the width *K* increases to nearly 10mm, the frequency regions of simultaneously negative ρ_{eff} and B_{eff} (claret-colored areas) appear for the first and second order HFAM. Hence, the double negativity of ρ_{eff} and B_{eff} can be designed and obtained in broadband frequency range by varying the width *K*. This provides a good candidate for future

research on acoustic negative refraction [27].

By comparing and analyzing the effective parameters of HFAM units, we can see the following three points. First, the proposed HFAM can create double negativity characteristic, in which monopolar resonance induced negative bulk modulus and the dipolar resonance generated negative mass density. Second, both ρ_{eff} and B_{eff} of HFAM are sensitive to the *Hilbert curve* channel K, so acoustic characteristic can be regulated and controlled. Meanwhile, the first two orders HFAM with simultaneously negative ρ_{eff} and B_{eff} can be accomplished by changing the width size K. Third, for the third order HFAM, the normalized frequency of the lowest effective parameter is [0.086, 0.129], which is far less than 1. Therefore, the higher order HFAM maybe effectively capable of sound blocking on a deep-subwavelength scale.

3.3. Density-near-zero of HFAMs: $\rho_{eff} \approx 0$

As one of the effective dynamic parameters of AMs, ρ_{eff} can approach zero in a specific frequency region. This density-near-zero AMs has many unique applications, such as perfect transmission with sharp bends and corners [57], sound cloaking [24,57] and tunneling [24,32,57]. We demonstrate that ρ_{eff} of HFAMs can facilitate sound propagation at the frequency where its ρ_{eff} tends to zero. To prove the $\rho_{eff}\approx 0$ of HFAMs, Fig. 7(a) shows the schematic setup which is used to retrieve $\rho_{eff}\approx 0$ of the first order HFAMs. We retrieve the four locations pressures P_{x1}, P_{x2}, P_{x3} and P_{x4} by carefully arranging HFAMs units based on the complex transmission (T) and reflection (R) coefficients [58]. In this approach, $\rho_{eff}\approx 0$ is obtained from the S-parameters for a plane wave normally incident on HFAMs units. The T and R are expressed in terms of the pressures at four locations using Eq. (7), respectively.

$$R = \frac{P_{x2}e^{-jkS_1} - P_{x1}}{P_{x1} - P_{x2}e^{jkS_1}},\quad T = \frac{\sin(kS_1)}{\sin(kS_2)}\frac{P_{x3}e^{jkS_2} - P_{x4}}{P_{x1} - P_{x2}e^{-jkS_1}}e^{jk(L_1+L_2)}, \tag{7}$$

where $k=\omega/c_0$ is the corresponding wave number in air. By inverting Eq. (7), we obtain the acoustic impedance Z and the refractive index n,

$$Z = \frac{r}{1-2\cdot R+R^2-T^2},\quad n = \frac{-j\cdot \log x}{k\cdot d}, \tag{8}$$

$$r = \pm\sqrt{(R^2-T^2-1)^2-4\cdot T^2},\quad x = \frac{1-R^2+T^2+r}{2\cdot T}, \tag{9}$$

The ρ_{eff} relative to the background air can be obtained from above n and Z [61].

$$\rho_{eff} = Z\cdot n/\rho_0 \tag{10}$$

Fig. 7(b)-(d) represent the retrieved real and imaginary part of ρ_{eff}. In Fig. 7(b) and (c), the real parts ρ_{eff} occur a dip, which are both equal to zero at the normalized frequencies 0.2843 and 0.1890, respectively. Fig. 7(d) displays the real ρ_{eff} of the third HFAM with respect to the normalized frequency. In the normalized frequency range from 0.1510 to 0.1545, real ρ_{eff} changes from positive to negative and crosses zero at 0.1537.

To further investigate the effect of $\rho_{eff}\approx 0$, the sound transmissions at density-near-zero frequency are calculated in Fig. 8. Fig. 8(a)-(c) show that the transmission coefficients approximatively reach 100%, when the normalized frequencies of the incident waves are 0.2843, 0.1890 and 0.1537, respectively. The density-near-zero AMs have been demonstrated that their transmissions should be a quasi-static process with an infinitely large phase velocity [3,59]. Thus, the spatial phase of the transmitted wave should keep constant, i.e. zero-phase-difference. The insets of Fig. 8(a)-(c) present the pressure field distributions at 0.2843, 0.1890 and 0.1537, in which the transmitted waves achieve the zero-phase-difference. These results imply that the perfect transmissions are obtained at these frequencies, which are exactly the density-near-zero frequencies. Meantime, other total transmission also happens near density-near-zero frequency, as HFAM units are arranged sparsely, generating resonance coupling between adjacent units. However, the phase pattern of sound wave is altered at the interface between the air and HFAMs slabs presented in Fig. A (Appendix A). In addition, the effects of changes on the thicknesses of HFAMs slabs (for example, the first order HFAM) are considered in Fig. B (Appendix B).

As analyzed above, the proposed HFAM with density-near-zero constructed can

produce extraordinary transmission without any phase change. In the vicinity of the density-near-zero, ρ_{eff} is close to zero, which the zero-phase-difference of propagation of sound wave occurs. In addition, one can adjust the frequency range of density-near-zero of HFAM by changing the *Hilbert curve* channel according to specific requirements. Specifically, for the third order HFAM, the normalized frequency of density-near-zero is far less than 1. It indicates that the third order HFAM can be applied to phase regulation of sound wave on a deep-subwavelength scale. Therefore, HFAM maybe effectively capable of sound quarter bending, sound cloaking and tunneling on a subwavelength scale.

4. Results and discussions

4.1. Low-frequency sound blocking of HFAMs with negative effective parameters

Low-frequency sound blocking has been regarded as a challenging task in airborne sound regime, since the mass density law predicts the required weight of the structure to be excessive [60]. Recently, Mie-resonance AMs have been adopted to achieve high reflectivity at the monopole frequency [32]. Ref [46] has explored the single-unit of HFAM in the waveguide with filling ratio 95.6% for the sound attenuation based on the multi-bandgaps property. In this work, we show that multiple HFAM units enable to shield the low-frequency sound below 1200Hz by a monolayer sparse arrangement with a subwavelength thickness. In the region of negative effective parameters, sound waves are reflected, meaning the sound tranissions are perfectly blocked. In Fig. 9(a), (b) and (c), the width of rectangular waveguide is $12a_0$. The distance between centers of two adjacent HFAM units is $2a_0$. Therefore, the filling ratio along the x-direction is just $6a_0/12a_0$ =50%, which is almost half of the rate in Ref [46]. Therefore, the material consumption and construction cost maybe significantly reduced.

Fig. 9 displays that six HFAM units are uniformly distributed in a wide rectangular waveguide. Fig. 9(a), (b) and (c) show the sound pressure field distributions of the first,

second and third order HFAM with six units, when the plane wave of the frequencies 642 Hz, 424 Hz and 238 Hz radiates normally along the *y*-direction, respectively. They are located in the frequency ranges [609 Hz, 792 Hz], [411 Hz, 560 Hz] and [230 Hz, 269 Hz] in Fig. 5(b)-(d), the negative bulk modulus of the first, second and third order HFAM occur. It is observed that the sound energy is concentrated inside units and sound wave is partly blocked up due to the high reflection of HFAM near monopole resonance. In the outlet, the sound pressure levels decrease to -23 dB, -47 dB and -59 dB, which are smaller than the incident sound pressure (0 dB). Moreover, the transmission coefficients shown in Fig. 9(d), (e) and (f) as the green dash-dot curve is almost 28.7%, 7.4% and 5.3%. Furthermore, with the increase in the number of HFAM units, the sound blocking property will be improved in Fig. 9(d), (e) and (f). Particularly, for third order HFAM, there is also a dip near dipole resonance (481 Hz), indicating the negative mass density can block sound. Interestingly, except for the dips near monopole and dipole, other troughs (multi-bands with multipolar resonances [47]) are produced in Fig. 9(f). When the number of HFAM units increases from 3 to 12, the dip for monopolar resonance is blueshifted and the dip for dipolar resonance is redshifted (except for the first order) relative to the resonance of the single-unit cell. The blueshift and redshift originate from the diffraction coupling between adjacent units [32]. Besides, compared to the first two orders, the normalized frequencies of near the monopole and dipole resonance of the third HFAM are respectively 0.0763 and 0.1543, indicating that the third order HFAM can be effectively applied to block sound waves with much longer wavelengths.

Based on the discussion above, we can obtain that HFAM can effectively block the propagation of sound wave at a low-frequency range between monopolar and dipolar resonances by simply arranging AMs in an array. In addition, the monopole and dipole resonance frequencies can be changed with the size of *Hilbert curve K*, so the acoustic shielding frequency bands of HFAM are easily adjusted in subwavelength range. Furthermore, HFAM with the higher order capable of yielding sound blocking capabilities with much longer wavelength. Especially, near the monopole frequency of

the third order HFAM, it can control wavelengths up to almost 13 times larger than the lattice constant. Thus, it provides an efficient method to design the sound blocking by arranging the higher order HFAM with subwavelength thickness and light-weight in sparse arrays.

4.2. Superior performances of HFAMs with density-near-zero

The characteristic of AMs with density-near-zero can lead to the fantastic application like quarter bending, sound cloaking and tunneling [57]. For $\rho_{eff}\approx 0$, as the phase velocity $c_m=\sqrt{B_m/\rho_m}\to\infty$ and wave number $k_m=\omega/c_m\to 0$, which implies that the waves can travel through AMs to achieve the zero-phase-difference. The sound wavefront shaping with Hilbert fractal is performed only by FEM simulation in Ref [46]. In this work, $\rho_{eff}\approx 0$ is not only predicted by the effective medium theory, but also can be exploited in a range of acoustic applications. Here, we exhibit the acoustic radiation field characterizations of HFAMs made of periodical distributions in 2D waveguides. These characterizations are obtained by the same geometrical structures (Fig. 1) which are carefully arranged, as presented in Fig. (10)-(12). We suppose that incident waves impinge onto the slabs of HFAMs from the left ports, and the transmitted waves are observed at the right ports (upper ports).

4.2.1. Quarter bending transmission of HFAMs

Fig. 10(a) and (b) represent the transmission coefficients and pressure field distributions with density-near-zero of the first and second order HFAM inside quarter bending waveguides. It is clearly observed that the transmission coefficients exhibit two peaks almost reaching 100% at the normalized frequency 0.2844 and 0.1891, which are caused by density-near-zero in Fig. 7(b) and (c). The pressure field distributions at 0.2844 and 0.1891 are presented in the insets of Fig. 10(a) and (b), displaying the wave passes through the quarter corner almost without reflection, keeping its plane wavefront from exits of the upper side. Fig. 10(c) and (d) represent the transmission coefficients and pressure field distributions with density-near-zero of the third order HFAM.

Particularly, for the third order HFAMs, with the complexity of the high level configuration by the fractal feature, the incident sound waves experience longer paths inside the structure, resulting in a higher index and multi-band characteristic [46,47]. This means that density-near-zero maybe arise at other frequency ranges, like a higher normalized frequency 0.3050 in Fig. 10(d). The same characteristics also appear in sound cloaking and tunneling in Fig. 11(d) and Fig. 12(d). From the insets of Fig. 10(c) and (d), it is worth pointing out that zero-phase-difference effects were obtained, when the frequencies are 0.1535 and 0.3050, respectively. For comparison, right insets of Fig. 10 show the pressure field distributions using the same configuration without HFAMs, when the incoming waves with density-near-zero are incident. As observed, sound wavefronts in outlet waveguides are no longer plane. In addition, note that except for the peaks caused by density-near-zero, adjacent peaks also occur because of extraordinary sound transmission generated by the resonance of adjacent units [61]. Although both the incident and transmitted parts are plane waves, its phase pattern changes at the exiting parts. The phenomenon of changing phase distributions is proved in Fig. A in Appendix A.

4.2.2. Sound cloaking of HFAMs

Sound waves are normally incident on 2D waveguide from the left side, with a rigid obstacle existing inside HFAMs. The slabs are made of seven layers and the channel width with a_0 along the vertical y-direction and a_0 being its thickness along the x-direction. The transmission coefficients and pressure field distributions with density-near-zero of HFAMs with an embedded narrow channel determined by a perfect rigid wall are plotted in Fig. 11. In Fig. 11(a) and (b), the transmission coefficients exhibit two peaks at frequencies 0.2819 and 0.1888, which are induced by the density-near-zero in Fig. 7(b) and (c). The upper insets of Fig. 11(a) and (b) present the pressure field distributions, when sound wave with frequencies 0.2819 and 0.1888 through AMs with obstacle inside waveguides. These results indicate that rigid objects are hidden as if they did not exist.

For the third order HFAMs, sound cloaking effects also occur as shown in the upper insets of Fig. 11(c) and (d), when the frequencies of incident wave are 0.1543 and 0.3068, respectively. By contrast, the pressure field distributions for these cases are plotted in below insets of Fig. 11 when HFAMs are removed. A clear shadow cast by the rigid obstacle and a distorted wavefront can be observed, suggesting that the cloaking effect does not exist. In addition, due to the different arrangements pattern of HFAMs, the resonance between the units disappears or is not obvious with respect to the frequency of different sound waves. As shown in Fig. 11(c) and (d), the other peaks are not clearly visible compared to the first two orders. The same phenomenon also occurs in Fig. 12(c).

4.2.3. Sound tunneling of HFAMs

Sound waves can be "squeezed" and tunneled through narrow channels filled with density-near-zero AMs, showing that the incoming plane wavefront is replicated at the output part [3,59,61]. Sound tunneling effect has a characteristics of 100% sound transmission, it will also help to achieve the acoustic devices of high performance for non-destructive transmission. The two rectangular waveguides connected by a narrow channel with HFAMs are plotted in insets of Fig. 12. The left/right HFAMs slabs widths are $3a_0$, middle slabs width is $6a_0$ within the waveguide.

Fig. 12(a) and (b) display the transmission coefficients and pressure field distributions with density-near-zero of the first and second order HFAMs. We can find that they exhibit two peaks at the frequencies 0.2838 and 0.1887，in which the transmission coefficients are 99.5% and 99.7%. Meanwhile, sound wave energy coming from the left side can be transported to the right side, and the zero-phase-difference effects also occur in the upper insets of Fig. 12(a) and (b), when the incident wave frequencies are 0.2838 and 0.1887, respectively. It manifests that the sound wave efficiently tunnels through the narrow channel using the first two orders HFAMs. Fig. 12(c) and (d) describe the transmission coefficients and pressure field distributions with density-near-zero of the third order HFAMs. From the upper insets of Fig. 12(c) and (d),

it can be clearly observed that the sound wave passes through the narrow channel perfectly and keeps its phase same, when the incident wave frequencies are 0.1533 and 0.3048, respectively. In addition, for the lower-frequency, it is notable that sound tunneling appears at a frequency corresponding to a wavelength much larger than the narrow channel width a_0, i.e., at $\lambda \approx 6.5a_0$. For comparison, the incident wave with density-near-zero can penetrate the same narrow channel configurations without HFAMs, as shown in the below insets of Fig. 12, suggesting that most of the incident waves are reflected by the rigid wall with impedance mismatching, and the sound tunneling effects do not exist.

From the above discussion, the proposed HFAMs with density-near-zero obtained by effective medium theory have been demonstrated to realize zero-phase-difference effects, like quarter bending, sound cloaking and tunneling. The high transmissions generated by resonance between adjacent units are also proved to produce no zero-phase-difference effects in phase pattern. With an increase in the fractal order, the higher order HFAMs possesses longer paths, indicating this zero-phase-difference will emerge in more frequency ranges due to its multi-band characteristics and gradually shifts to the lower-frequency. These results also imply that the third order HFAMs can manipulate the waves propagation with wavelength nearly 6 times larger than lattice constant, i.e. on deep-subwavelength scale.

5. Conclusion

Inspired by the self-similar fractal configurations, *Hilbert curves* are applied to design a kind of the labyrinthine AMs. The numerical results have demonstrated that the proposed HFAM can motivate both the monopole and dipole modes, in which the monopole mode induces the negative bulk modulus and the dipole mode contributes to the negative density, respectively. Meanwhile, with the increase of the fractal order, the monopolar and bipolar resonances gradually shift to the lower frequency domain. Furthermore, based on the transfer matrix and *S*-parameter method, the negative mass density and bulk modulus, and the density-near-zero of HFAM are respectively

achieved. Although taking the air losses into consideration, the negative effective properties are obatined. In addition, the effects of *Hilbert curve* channel width on the resonant modes and effective parameters also have been thoroughly analyzed. Due to the unique negative property of HFAM, we developed a monolayer AMs with subwavelength thickness to block the sound propagation at the low-frequency range, e.g. 100-1200 Hz. We also showed that the appropriate arrangements of HFAMs in arrays have a perfect transmission in the density-near-zero, in which the zero-phase-difference effects are produced in sound wave regulations, for instance, quarter bending, sound cloaking and tunneling. Specially, with the increase of the fractal orders, the zero-phase-difference effects of the third order HFAMs not only obtain on deep-subwavelength scale, but also exhibit the multi-band characteristics. Our future work will include the fabrications of the proposed HFAM and experimental verification, as well as investigation of more perfect structures based on the demonstrated phenomena. These explorations, therefore, provide useful guidelines for the labyrinthine AMs to modulate the negative effective parameters and zero-phase-difference effects on subwavelength scale. The obtained novel properties can be further employed in the device applications of the future functional metamaterials.

Acknowledgement

The work was partially supported by Joint Found of Ministry of Education for Equipment Pre-Research (6141A02033216), and Australian Research Council (ARC) - Discovery Projects (160102491), as well as the CSC Scholarship (201706130093) and Hunan Provincial Innovation Foundation for Postgraduate Students (CX2016B080).

Appendix A. The resonance of HFAMs near density-near-zero

Due to coupling interaction of the adjacent units, it leads to the resonance, causing the extraordinary sound transmission [61]. As shown in Fig A, except for density-near-zero, when the normalized frequency is 0.2786, 0.1857 and 0.1550, respectively, the resonances occur and the high transmission coefficients of HFAM also

appear. The insets represent the pressure field distributions corresponding to their resonance frequencies. From the sound field distributions, it is clearly seen that their phases change near the two ends of HFAM. Note that although the high transmissions also occur by resonance of adjacent units, the zero-phase-difference effects are not produced.

Appendix B. The effect of HFAMs thickness on density-near-zero

To illustrate the effect of the thickness of HFAMs on density-near-zero, we take the first order HFAMs as an example to analyze their relation. We choose three thickness slabs ($7a_0$, $10a_0$ and $15a_0$) randomly as shown in Fig. B. When the slab is $10a_0$ in Fig. B(c) [same as Fig. 8(a)], the transmission coefficient shows one peak at the normalized frequency 0.2843 in Fig. B(d), in which sound field distribution as shown in Fig. B(c) [same as Fig. 8(a)]. When the slab is $7a_0$ shorter in Fig. B(a), the effect of local resonance between HFAM units becomes weaker, thus the frequency decreases in Fig. B(b). When the resonance units are enough, the frequency of the peak will close to the density-near-zero frequency. For example, when the slab is $15a_0$ in Fig. B(e), the peak appears at the normalized frequency 0.2843 again in Fig. B(f).

References

[1] Z. Yang, J. Mei, M. Yang, N.H. Chan, P. Sheng, Membrane-type acoustic metamaterial with negative dynamic mass, Phys. Rev. Lett. 101 (2008) 204301.

[2] N. Fang, D. Xi, J. Xu, M. Ambati, W. Srituravanich, C. Sun, X. Zhang, Ultrasonic metamaterials with negative modulus, Nat. Mater. 5 (2006) 452-456.

[3] R. Fleury, A. Alu, Extraordinary sound transmission through density-near-zero ultranarrow channels, Phys. Rev. Lett. 111 (2013) 055501.

[4] D.R. Smith, J.B. Pendry, M.C. Wiltshire, Metamaterials and negative refractive index, Science 305 (2004) 788-792.

[5] M. Mohsenizadeh, F. Gasbarri, M. Munther, A. Beheshti, K. Davami, Additively-manufactured lightweight Metamaterials for energy absorption, Mater. Design. 139 (2018) 521-530.

[6] S. Qi, Y. Li, B. Assouar, Acoustic focusing and energy confinement based on multilateral metasurfaces, Phys. Rev. Appl. 7 (2017).

[7] P. Bai, X. Yang, X. Shen, X. Zhang, Z. Li, Q. Yin, G. Jiang, F. Yang, Sound absorption performance of the acoustic absorber fabricated by compression and microperforation of the porous metal, Mater. Design. 167 (2019) 107637.

[8] G. Ma, M. Yang, S. Xiao, Z. Yang, P. Sheng, Acoustic metasurface with hybrid resonances, Nat. Mater. 13 (2014) 873-878.
[9] M. Yang, S. Chen, C. Fu, P. Sheng, Optimal sound-absorbing structures, Mater. Horiz 4 (2017) 673-680.
[10] S. Zhang, C. Xia, N. Fang, Broadband acoustic cloak for ultrasound waves, Phys. Rev. Lett. 106 (2011).
[11] S.A. Cummer, J. Christensen, A. Alù, Controlling sound with acoustic metamaterials, Nat. Rev. Mater. 1 (2016) 16001.
[12] J. Li, L. Fok, X. Yin, G. Bartal, X. Zhang, Experimental demonstration of an acoustic magnifying hyperlens, Nat. Mater. 8 (2009) 931-934.
[13] L. Zigoneanu, B.I. Popa, S.A. Cummer, Design and measurements of a broadband two-dimensional acoustic lens, Phys. Rev. B 84 (2011).
[14] B.Z. Xia, T.T. Liu, G.L. Huang, H.Q. Dai, J.R. Jiao, X.G. Zang, D.J. Yu, S.J. Zheng, J. Liu, Topological phononic insulator with robust pseudospin-dependent transport, Phys. Rev. B 96 (2017).
[15] Z. Liu, X. Zhang, Y. Mao, Y.Y. Zhu, Z. Yang, C.T. Chan, P. Sheng, Locally resonant sonic materials, Science 289 (2000) 3.
[16] H. Chen, C.T. Chan, P. Sheng, Transformation optics and metamaterials, Nat. Mater. 9 (2010) 387-396.
[17] M. Farhat, S. Enoch, S. Guenneau, A.B. Movchan, Broadband cylindrical acoustic cloak for linear surface waves in a fluid, Phys. Rev. Lett. 101 (2008) 134501.
[18] J. Li, C.T. Chan, Double-negative acoustic metamaterial, Phys. Rev. E, 70 (2004) 055602.
[19] S.H. Lee, C.M. Park, Y.M. Seo, Z.G. Wang, C.K. Kim, Composite acoustic medium with simultaneously negative density and modulus, Phys. Rev. Lett. 104 (2010) 054301.
[20] S.H. Lee, C.M. Park, Y.M. Seo, Z.G. Wang, C.K. Kim, Acoustic metamaterial with negative density, Phys. Lett. A 373 (2009) 4464-4469.
[21] S.H. Lee, C.M. Park, Y.M. Seo, Z.G. Wang, C.K. Kim, Acoustic metamaterial with negative modulus, J. Phys.: Condens. Matter 21 (2009) 175704.
[22] J. Christensen, Z. Liang, M. Willatzen, Metadevices for the confinement of sound and broadband double-negativity behavior, Phys. Rev. B 88 (2013).
[23] Z. Yang, J. Mei, M. Yang, N. Chan, P. Sheng, Membrane-type acoustic metamaterial with negative dynamic mass, Phys. Rev. Lett. 101 (2008) 204301.
[24] Z.X. Liang, J. Li, Extreme acoustic metamaterial by coiling up space, Phys. Rev. Lett. 108 (2012) 114301.
[25] Y. Li, B. Liang, X. Tao, X.F. Zhu, X.Y. Zou, J.C. Cheng, Acoustic focusing by coiling up space, Appl. Phys. Lett. 101 (2012) 233508.
[26] Z.X. Liang, T.H. Feng, S. Lok, F. Liu, K.B. Ng, C.H. Chan, J.J. Wang, S. Han, S. Lee, J. Li, Space-coiling metamaterials with double negativity and conical dispersion, Sci. Rep. 3 (2013) 1614.
[27] Y.B. Xie, B.I. Popa, L. Zigoneanu, S.A. Cummer, Measurement of a broadband negative index with space-coiling acoustic metamaterials, Phys. Rev. Lett. 110 (2013) 175501.
[28] Y.B. Xie, A. Konneker, B.I. Popa, S.A. Cummer, Tapered labyrinthine acoustic metamaterials for broadband impedance matching, Appl. Phys. Lett. 103 (2013) 201906.
[29] T. Frenzel, D.B. Jan, T. Bückmann, R. Schittny, M. Kadic, M. Wegener, Three-dimensional labyrinthine acoustic metamaterials, Appl. Phys. Lett. 103 (2013) 061907.

[30] S.K. Maurya, A. Pandey, S. Shukla, S. Saxena, Double negativity in 3D space coiling metamaterials, Sci. Rep. 6 (2016) 33683.
[31] C. Zhang, X. Hu, Three-dimensional single-port labyrinthine acoustic metamaterial: perfect absorption with large bandwidth and tunability, Phys. Rev. Appl. 6 (2016).
[32] Y. Cheng, C. Zhou, B.G. Yuan, D.J. Wu, Q. Wei, X.J. Liu, Ultra-sparse metasurface for high reflection of low-frequency sound based on artificial Mie resonances, Nat. Mater. 14 (2015) 1013-1019.
[33] A.O. Krushynska, F. Bosia, M. Miniaci, N.M. Pugno, Spider web-structured labyrinthine acoustic metamaterials for low-frequency sound control, New. J. Phys. 19 (2017) 105001.
[34] J. Zhang, Y. Cheng, X.J. Liu, Extraordinary acoustic transmission at low frequency by a tunable acoustic impedance metasurface based on coupled Mie resonators, Appl. Phys. Lett. 110 (2017) 233502.
[35] X.F. Zhu, B. Liang, W.W. Kan, Y.G. Peng, J.C. Cheng, Deep-subwavelength-scale directional sensing based on highly localized dipolar Mie Rrsonances, Phys. Rev. Appl. 5 (2016).
[36] G.X. Lu, E. Ding, Y.Y. Wang, X.Y. Peng, J. Cui, X.Z. Liu, X.J. Liu, Realization of acoustic wave directivity at low frequencies with a subwavelength Mie resonant structure, Appl. Phys. Lett. 110 (2017) 123507.
[37] X.F. Fu, G.Y. Li, M.H. Lu, G. Lu, X. Huang, A 3D space coiling metamaterial with isotropic negative acoustic properties, Appl. Phys. Lett. 111 (2017) 251904.
[38] R. Oftadeh, B. Haghpanah, D. Vella, A. Boudaoud, A. Vaziri, Optimal fractal-like hierarchical honeycombs, Phys. Rev. Lett. 113 (2014) 104301.
[39] D. Mousanezhad, S. Babaee, R. Ghosh, E. Mahdi, K. Bertoldi, A. Vaziri, Honeycomb phononic crystals with self-similar hierarchy, Phys. Rev. B 92 (2015).
[40] A.S. Fallah, N. Navadeh, V.V. Tereshchuk, V.N. Gorshkov, Phononic dispersion in anisotropic pseudo-fractal hyper-lattices, Mater. Design. 164 (2019) 107560.
[41] N.K. Kuo, G. Piazza, Fractal phononic crystals in aluminum nitride: An approach to ultra high frequency bandgaps, Appl. Phys. Lett. 99 (2011) 163501.
[42] G.Y. Song, Q. Cheng, B. Huang, H.Y. Dong, T.J. Cui, Broadband fractal acoustic metamaterials for low-frequency sound attenuation, Appl. Phys. Lett. 109 (2016) 131901.
[43] G.Y. Song, B. Huang, H.Y. Dong, Q. Cheng, T.J. Cui, Broadband focusing acoustic lens based on fractal metamaterials, Sci. Rep. 6 (2016) 35929.
[44] B.Z. Xia, L.P. Li, J. Liu, D.J. Yu, Acoustic metamaterial with fractal coiling up space for sound blocking in a deep subwavelength scale, ASME J. Vib. Acoust. 140 (2017) 011011.
[45] J. Liu, L.P. Li, B.Z. Xia, X.F. Man, Fractal labyrinthine acoustic metamaterial in planar lattices, Int. J. Solids Struct. 132-133 (2018) 20-30.
[46] X.F. Man, T.T. Liu, B.Z. Xia, Z. Luo, L.X. Xie, J. Liu, Space-coiling fractal metamaterial with multi-bandgaps on subwavelength scale, J. Sound. Vib. 423 (2018) 322-339.
[47] A.O. Krushynska, F. Bosia, N.M. Pugno, Labyrinthine acoustic metamaterials with space-coiling channels for low-frequency sound control, Acta Acust. united Ac 104 (2018) 200-210.
[48] M. Miniaci, A. Krushynska, A.S. Gliozzi, N. Kherraz, F. Bosia, N.M. Pugno, Design and fabrication of bioinspired hierarchical dissipative elastic metamaterials, Phys. Rev. Appl. 10 (2018).
[49] X. Zhao, G. Liu, C. Zhang, D. Xia, Z. Lu, Fractal acoustic metamaterials for transformer noise reduction, Appl. Phys. Lett. 113 (2018) 074101.

[50] X.F. Man, B.Z. Xia, Z. Luo, J. Liu, 3D Hilbert fractal acoustic metamaterials: low-frequency and multi-band sound insulation, J. Phys. D: Appl. Phys. 52 (2019) 195302.
[51] Y.Y. Chen, L.F. Wang, Multiband wave filtering and waveguiding in bio-inspired hierarchical composites, Extreme Mech. Lett. 5 (2015) 18-24.
[52] P. Zhang, A.C. To, Broadband wave filtering of bioinspired hierarchical phononic crystal, Appl. Phys. Lett. 102 (2013) 121910.
[53] B.B. Mandelbrot, The fractal geometry of nature, W.H. Freeman & Company, New York, 1983.
[54] M. Molerón, M. Serra-Garcia, C. Daraio, Visco-thermal effects in acoustic metamaterials: from total transmission to total reflection and high absorption, New. J. Phys. 18 (2016) 033003.
[55] B.H. Song , J.S. Bolton, A transfer-matrix approach for estimating the characteristic impedance and wave numbers of limp and rigid porous materials, J. Acoust. Soc. Am. 107 (2000) 22.
[56] P. Li, S.S. Yao, X.M. Zhou, G.L. Huang, G.K. Hu, Effective medium theory of thin-plate acoustic metamaterials, J. Acoust. Soc. Am. 135 (2014) 1844-1852.
[57] R. Graciá-Salgado, V.M. García-Chocano, D. Torrent, J. Sánchez-Dehesa, Negative mass density and ρ-near-zero quasi-two-dimensional metamaterials: Design and applications, Phys. Rev. B 88 (2013).
[58] V. Fokin, M. Ambati, C. Sun, X. Zhang, Method for retrieving effective properties of locally resonant acoustic metamaterials, Phys. Rev. B 76 (2007).
[59] Y. Gu, Y. Cheng, J.S. Wang, X.J. Liu, Controlling sound transmission with density-near-zero acoustic membrane network, J. Appl. Phys. 118 (2015) 024505.
[60] Z. Yang, H.M. Dai, N.H. Chan, G.C. Ma, P. Sheng, Acoustic metamaterial panels for sound attenuation in the 50–1000 Hz regime, Appl. Phys. Lett. 96 (2010) 041906.
[61] L.Y. Zheng, Y. Wu, X. Ni, Z.G. Chen, M.H. Lu, Y.F. Chen, Acoustic cloaking by a near-zero-index phononic crystal, Appl. Phys. Lett. 104 (2014) 161904.

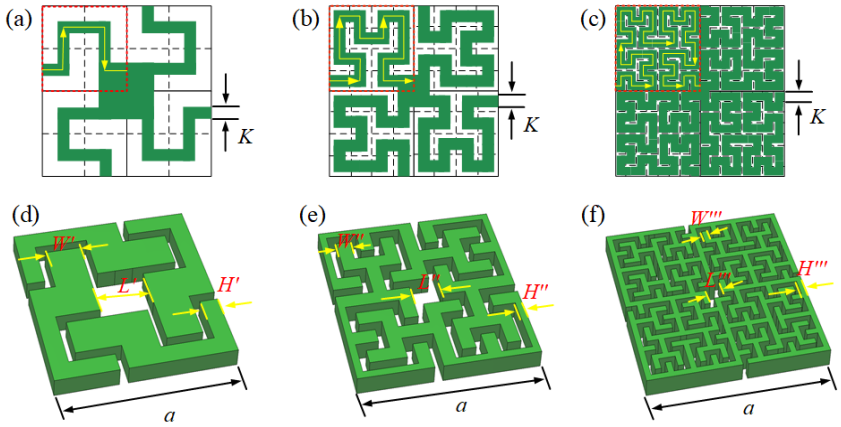

Fig. 1. Schematic cross-sectional illustrations of three types of unit cells of HFAM:(a)-(c) The *Hilbert curve* channel of the first to third order HFAM with fluid. (d)-(f) The oblique drawing of unit cells of the first to third order HFAM. The material of HFAM applied is epoxy resin. The geometric and property parameters of HFAM are listed: a=105mm, K=5mm; H'= 10.625mm, H''= 4.0625mm, H'''= 0.7812mm; W'=21.25mm, W''=8.125mm, W'''=1.5625mm; ρ_1=1050kg/m^3, c_1=2500m/s and ρ_0=1.25kg/m^3, c_0=343m/s.

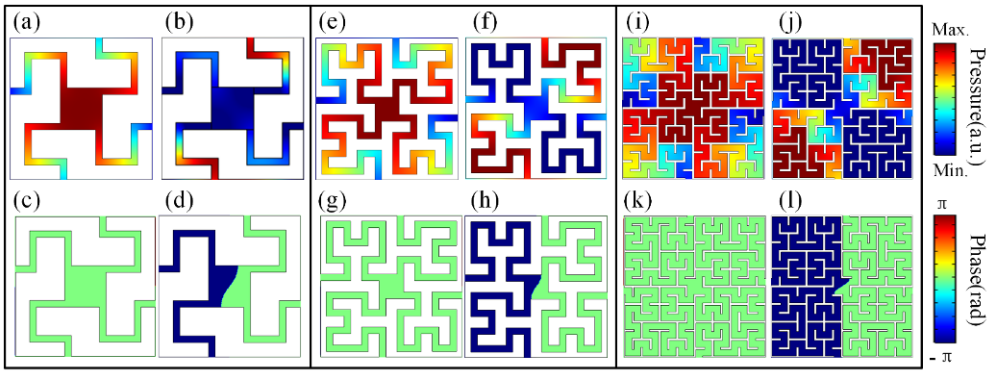

Fig. 2. Field distributions of HFAM eigenstate modes. (a)–(l) Acoustic modes of the artificial monopole and dipole, respectively. The first and second rows depict the pressure and phase fields distributions of the first to third order HFAM (dark blue and deepred represent small and large values), respectively.

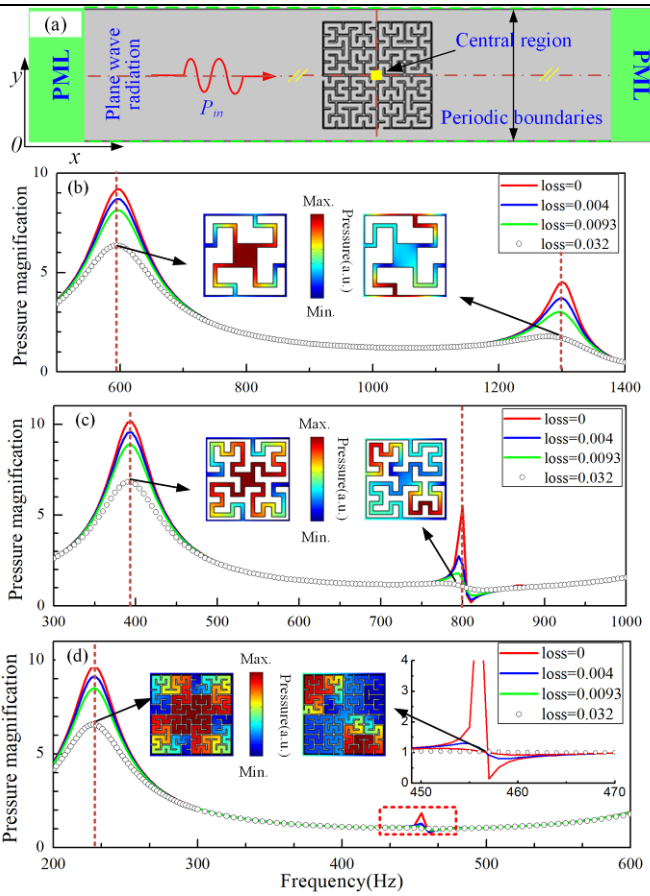

Fig. 3. (a) Schematic diagram of HFAM calculating pressure magnification (for example, yellow area of the third order HFAM). (b)-(d) The pressure magnifications of monopole and dipole modes of the first to third order HFAM with respect to various losses. The middle insets show the pressure fields of HFAM units. The right inset in Fig. 3(d) shows enlarged drawing pressure magnification of the third order HFAM at dipole resonance.

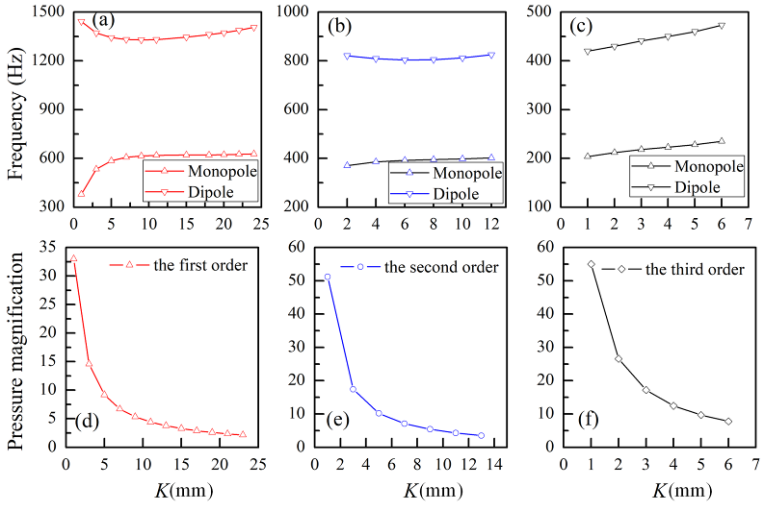

Fig. 4. (a)-(c) Variations of the monopole and dipole resonance frequencies of the first to third order HFAMs with respect to *Hilbert curve* channels *K*. (d)-(f) The relationship between the pressure amplification corresponding to monopole resonance and *K* in lossless air.

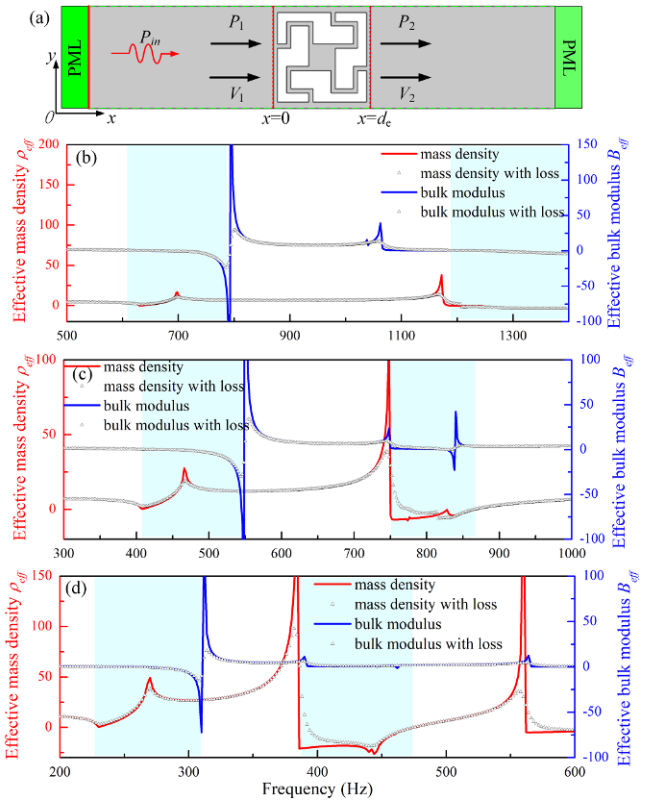

Fig. 5. (a) Schematic diagram of the transfer matrix method. (b)-(d) Effective parameters (ρ_{eff} and B_{eff}) for units of the first, second and third order HFAM. The red solid and blue solid curve show the ρ_{eff} and B_{eff} of HFAM units, respectively. The black hollow and circle triangulars represent the ρ_{eff} and B_{eff} with loss=0.0093, respectively.

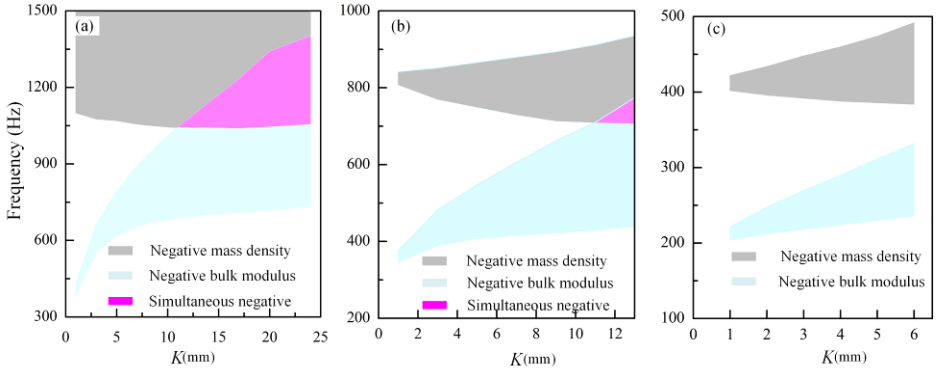

Fig. 6. The relationship between negative ρ_{eff} and B_{eff} of the first order HFAM (a), the second order HFAM (b), the third order HFAM (c) and *Hilbert curve* channel K in the lossless air.

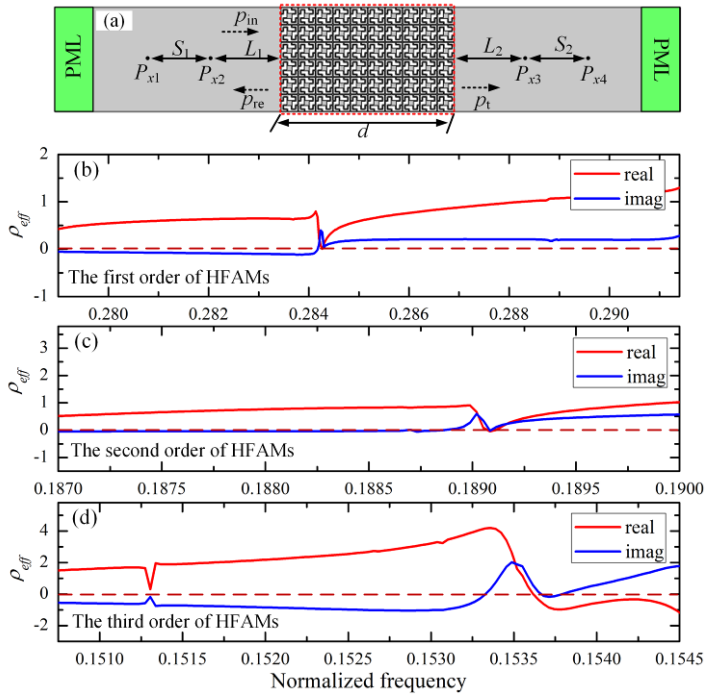

Fig. 7. (a) Schematic diagram of the *S*-parameter method. The thickness and height of HFAMs are $d=10a_0=1.1$ m and $6a_0=0.66$ m. The four distances are $S_1=S_2=0.598$ m and $L_1=L_2=0.55$ m, respectively. (b)-(d) The real part (red solid line) and imaginary part curves (blue solid line) of ρ_{eff} of HFAMs.

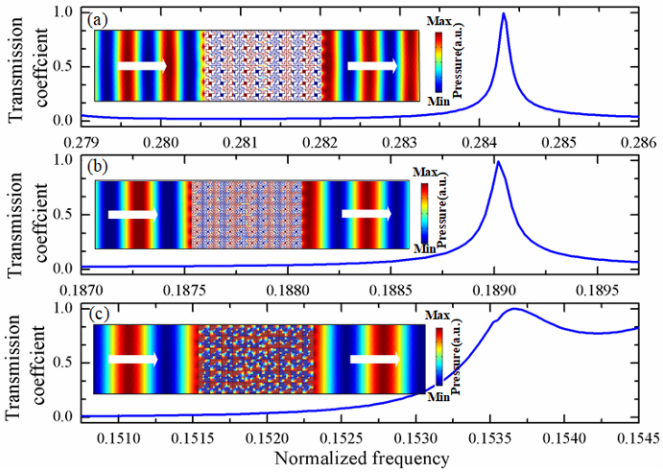

Fig. 8. (a)-(c) Transmission coefficients of the first to third order HFAMs when inserted into a waveguide. The insets represent sound pressure field distributions of HFAMs when the incident waves are at the density-near-zero frequency, respectively. The white arrows represent the propagation direction of sound waves.

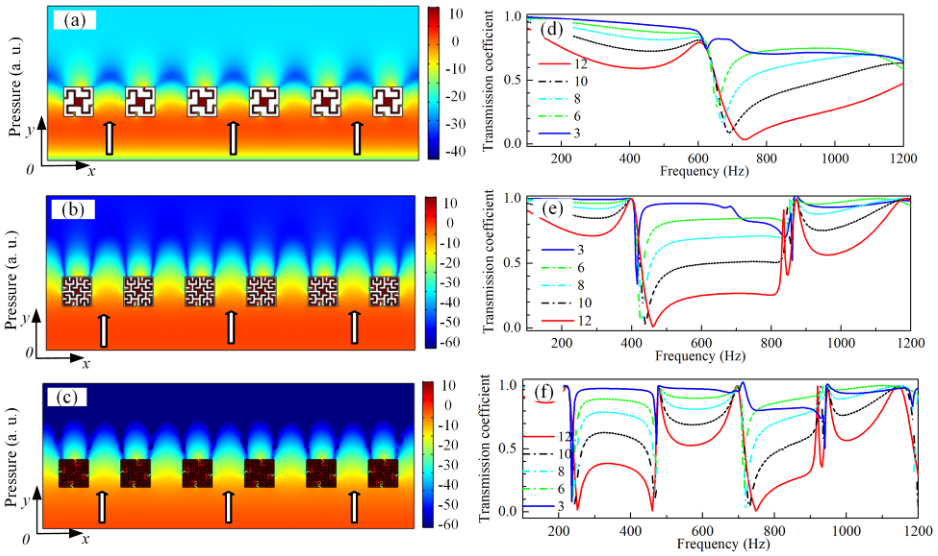

Fig. 9. (a)-(c) Sound pressure field distributions with six units of the first, second and third order HFAMs in a wide rectangular waveguide. (d)-(f) the transmission coefficients of the first, second and third order HFAMs in a wide rectangular waveguide, when the numbers of HFAMs units are 3, 6, 8, 10 and 12, respectively.

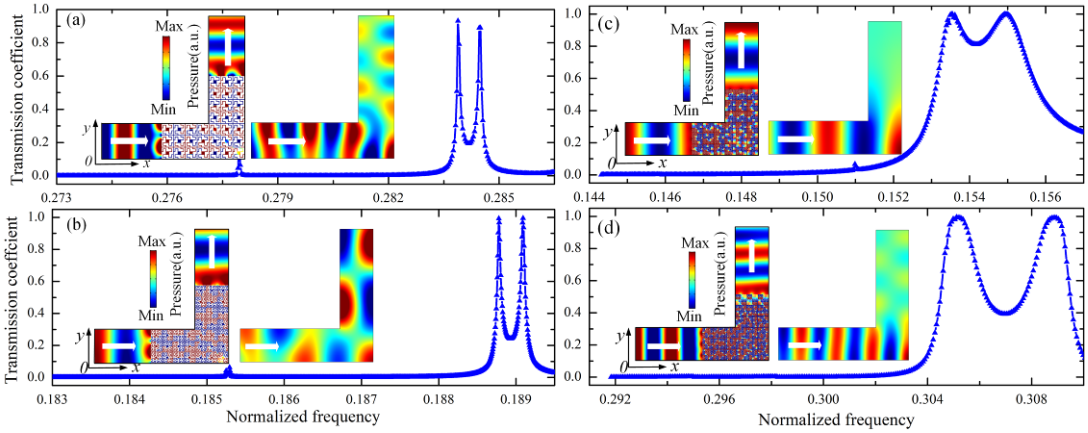

Fig. 10. (a) and (b) Transmission coefficients and pressure field distributions with density-near-zero of the first and second order HFAMs within a 90º waveguide. (c) and (d) Transmission coefficients and pressure field distributions with density-near-zero of the third order HFAMs within a 90º waveguide.

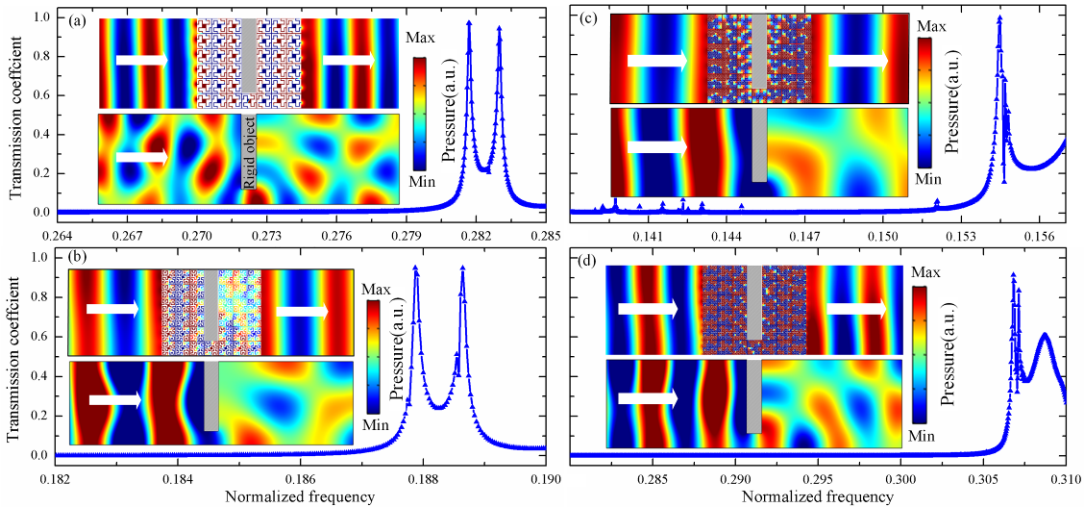

Fig. 11. (a) and (b) Transmission coefficients and pressure maps with density-near-zero showing the sound propagation through a rectangle rigid obstacle surrounded by the first and second order HFAMs. (c) and (d) Transmission coefficients and pressure maps with density-near-zero showing the sound propagation through a rectangle rigid obstacle surrounded by the third order HFAMs.

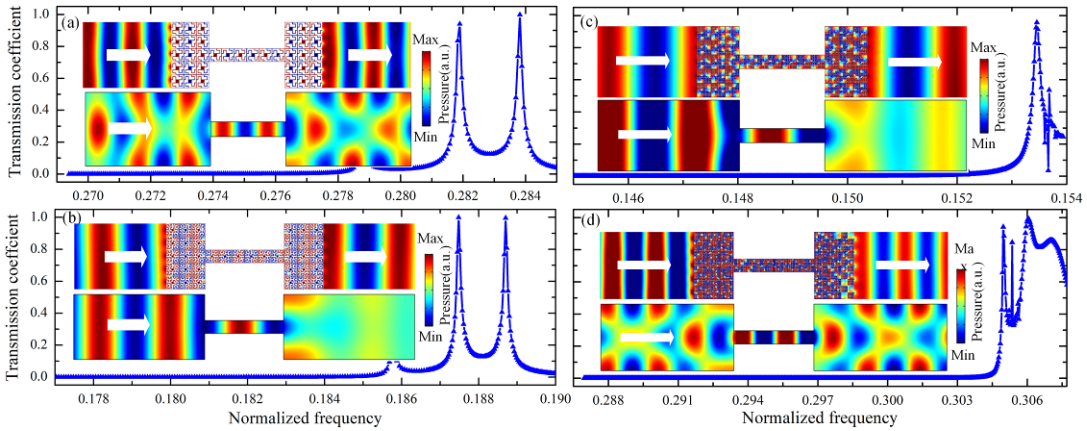

Fig. 12. (a) and (b) Transmission coefficients and pressure field distributions with density-near-zero of a narrow channel surrounded by the first and second order HFAMs. (c) and (d) Transmission coefficients and pressure field distributions with density-near-zero of a narrow channel surrounded by the third order HFAMs.

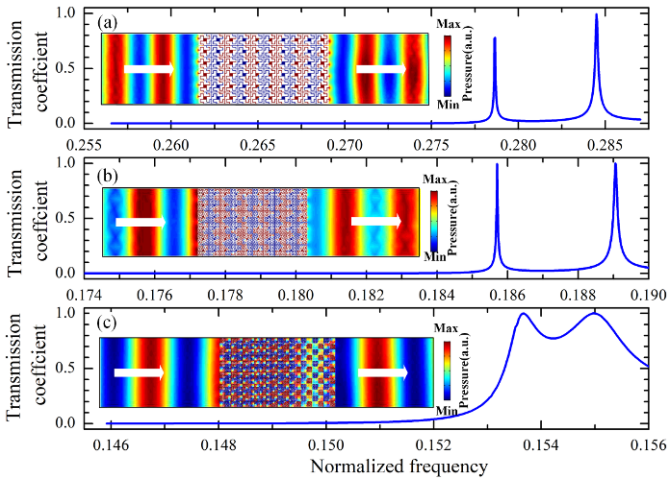

Fig. A. (a)-(c) Transmission coefficients of the first to third order HFAMs when inserted into a waveguide. The insets represent pressure field distributions of HFAMs when the incident wave is at resonance frequency near the density-near-zero, respectively.

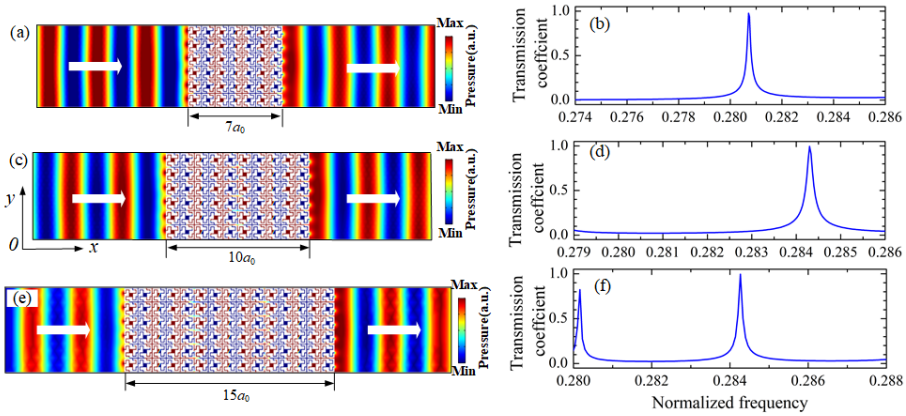

Fig. B. (a), (c) and (e) Sound pressure field distributions of the first order HFAMs with the width $7a_0$, $10a_0$ and $15a_0$, when the incident waves at the normalized frequencies 0.2807, 0.2843 and 0.2843, respectively. (b), (d) and (f) The transmission coefficients of the slabs of first order HFAMs with the width is $7a_0$, $10a_0$ and $15a_0$, respectively.